

This document is confidential and is proprietary to the American Chemical Society and its authors. Do not copy or disclose without written permission. If you have received this item in error, notify the sender and delete all copies.

**Optimizing The Activity of Nano-needle Structured WO₃
Photoanodes for Solar Water Splitting – Direct Synthesis Via
Chemical Vapor Deposition**

Journal:	<i>The Journal of Physical Chemistry</i>
Manuscript ID	jp-2017-00533u.R1
Manuscript Type:	Article
Date Submitted by the Author:	n/a
Complete List of Authors:	Kafizas, Andreas; Imperial College London, Chemistry Francàs, Laia; Imperial College London Sotelo-Vazquez, Carlos; University College London Ling, Min; University College London, Li, Yaomin; University College London Glover, Emily; University College London McCafferty, Liam; University College London Blackman, Christopher; University College London, Chemistry Darr, Jawwad; University College London, Department of Chemistry Parkin, Ivan; UCL, Chemistry

SCHOLARONE™
Manuscripts

Optimizing The Activity of Nano-needle Structured WO₃ Photoanodes for Solar Water Splitting – Direct Synthesis *Via* Chemical Vapor Deposition

Andreas Kafizas,^[a]* Laia Francàs,^[a] Carlos Sotelo-Vazquez,^[b] Min Ling,^[b] Yaomin Li,^[b] Emily Glover,^[b] Liam McCafferty,^[b] Chris Blackman,^[b] Jawwad Darr^[b] and Ivan Parkin^[b]

[a] Department of Chemistry, Imperial College London, SW7 2AZ

[b] Department of Chemistry, University College London, WC1H 0AJ

ABSTRACT: Solar water splitting is a promising solution for the renewable production of hydrogen as an energy vector. To date, complex or patterned photoelectrodes have shown the highest water splitting efficiencies, but lack scalable routes for commercial scale-up. In this article, we report a direct and scalable chemical vapor deposition (CVD) route at atmospheric pressure, for a single step fabrication of complex nano-needle structured WO₃ photoanodes. Using a systematic approach, the nanostructure was engineered to find the conditions that result in optimal water splitting. The nanostructured materials adopted a monoclinic γ -WO₃ structure and were highly oriented in the (002) plane, with the nano-needle structures stacking perpendicular to the FTO substrate. The WO₃ photoanode that showed the highest water splitting

1
2
3 activity was composed of a ~300 nm seed layer of flat WO₃ with a ~5 μm thick top layer of WO₃
4 nano-needles. At 1.23 V_{RHE}, this material showed incident photon-to-current efficiencies in the
5 range ~35 – 45 % in the UV region (250 – 375 nm) and an overall solar predicted photocurrent
6 of 1.24 mA.cm⁻² (~25 % of the theoretical maximum for WO₃). When coupled in tandem with a
7 photovoltaic device containing a methyl ammonium lead iodide perovskite, a solar-to-hydrogen
8 efficiency of *ca* 1 % for a complete unassisted water splitting device is predicted.
9
10
11
12
13
14
15
16
17
18

19 INTRODUCTION

20
21 It is widely acknowledged that the release of CO₂ from the combustion of fossil fuels is one of
22 the primary causes of *Global Warming* – an effect that has resulted in increased average
23 temperatures, melted polar ice and risen sea levels.^{1,2} Sunlight has the potential to be our largest
24 energy source, the amount reaching the Earth's surface each hour being almost twice the total
25 energy consumed annually from fossil fuels, nuclear and all other renewable energy sources
26 combined.³ Consequently, solar cells are the fastest growing renewable technology. However,
27 the biggest barrier to photovoltaics is the unpredictability of sunlight coupled with the mismatch
28 between the times they work best and the times we need energy the most.⁴ This is a major
29 problem, as most electrical energy produced by photovoltaics must be used at the point of
30 generation, as there is currently no integrated means of storing this energy.⁵
31
32
33
34
35
36
37
38
39
40
41
42
43
44

45 Photosynthesis is the perfect example of how plants use sunlight to produce fuel, which can be
46 stored and used when required. This has resulted in many bio-inspired approaches – deemed
47 *artificial photosynthesis*⁶ – where arguably the most promising approach is the solar driven
48 photolysis of water to produce hydrogen fuel from water using semiconductor photoelectrodes.⁷
49 Numerous semiconductor materials have been examined for photoelectrochemical water
50 splitting,⁸ where metal oxides generally show several distinct advantages over other materials
51
52
53
54
55
56
57
58
59
60

1
2
3 (e.g. high resistance to photocorrosion in water, low toxicity, low synthetic cost and
4 compatibility with up-scale). Some of the most promising metal oxide photoelectrodes include α -
5 Fe_2O_3 ,⁹ BiVO_4 ,¹⁰ TiO_2 ¹¹ and WO_3 .¹²⁻¹⁹ WO_3 ($E_{\text{bg}} \sim 2.7$ eV, photocurrent onset ~ 0.5 V_{RHE})¹⁸ is an
6 promising candidate as it can absorb more of the solar spectrum than TiO_2 (3.0 eV, ~ 0.2 V_{RHE}),¹¹
7 begins to function at a lower onset potential than both BiVO_4 (2.4 eV, ~ 0.8 V_{RHE})^{20,21} and α -
8 Fe_2O_3 (2.1 eV, ~ 0.9 V_{RHE})^{9,22} and is stable at low pH where H_2 evolution is often more
9 efficient.²³ WO_3 photoanodes have been fabricated using numerous techniques, including sol-gel,
10 hydrothermal, solvothermal, electrochemical, spray pyrolysis and physical sputtering methods,¹⁷
11 and have reached current densities as high as $2.4 \text{ mA}\cdot\text{cm}^{-2}$ at 1.23 V_{RHE} ¹⁴ under 1 sun
12 illumination (~ 50 % of the theoretical maximum) showing a Faradaic efficiency of ~ 50 %.
13 Similarly high current densities have been achieved in complete unassisted tandem cell devices
14 composed of WO_3 photoanodes grown using a sol-gel method, coupled with a dye-sensitized
15 solar cell.²⁴ Other studies have shown that the light absorption characteristics of WO_3 can be
16 improved by intercalating Na or N_2 dopants^{12,19} or by coupling with a semiconductor of narrower
17 bandgap such as BiVO_4 ²⁵⁻²⁷ or $\alpha\text{-Fe}_3\text{O}_4$.²⁸

18
19
20
21
22
23
24
25
26
27
28
29
30
31
32
33
34
35
36
37
38
39
40
41
42
43
44
45
46
47
48
49
50
51
52
53
54
55
56
57
58
59
60
Given the promise that WO_3 photoanodes have shown, there have been few studies detailing
how complex WO_3 structures and coatings can be grown using an industrially applicable method.
Many of the current methods to create complex or patterned coatings such as lithography are
often laborious and time consuming, involving pattern, deposit and etch steps.²⁹ In this article,
we demonstrate how complex nano-needle structures of WO_3 can be grown using an industrially
applicable route, chemical vapor deposition (CVD). Importantly, CVD routes are highly scalable
and can be applied to continuous fabrication or roll-to-roll processes, and is currently used
heavily in industry to grow films and coatings on a large scale.³⁰ In the past, WO_3 photoanodes

1
2
3 have been grown using low-pressure CVD methods that are inherently less upscalable due to the
4 requirement for low pressure.^{31,32} They have also been grown using a flame CVD method at
5 atmospheric pressure,¹⁵ but required the use of a WO₃ seed layer that was first grown using a sol-
6 gel method. In this article, we adapt an aerosol-assisted CVD method, previously used to grow
7 WO₃-based gas sensing devices at atmospheric pressure.^{33,34} The method was adapted so that
8 combinations of flat or stacked nano-needle structures could be grown in two steps at different
9 temperatures. These flat structures acted as a seed layer for growing more densely packed nano-
10 needle structures. The effect of layer thickness for flat, nano-needle and combinations of the two
11 structures were systematically studied. This allowed us to understand the relationship between a
12 tailored nanostructure and material thickness for optimal light absorption and water splitting
13 activity. The water splitting behavior of the best performing sample was characterized in depth,
14 including its predicted performance when coupled in tandem with a photovoltaic cell containing
15 a perovskite, methyl ammonium lead iodide, to form an unassisted water splitting device.
16
17
18
19
20
21
22
23
24
25
26
27
28
29
30
31
32
33
34
35
36

37 EXPERIMENTAL SECTION

38
39
40
41 **Materials synthesis:** WO₃ photoanodes were grown using an aerosol-assisted chemical vapor
42 deposition (AACVD) process at atmospheric pressure (Figure S1a), using an adapted method to
43 that previously reported by Blackman *et al.*³³ A picture of the AACVD apparatus is shown in
44 Figure S1b. All materials were grown on FTO substrates (2.5 x 2.7 cm). The substrates were
45 heated from underneath using a graphite heating block. The inlet to the reactor was equipped
46 with a cooling water jacket. This was to prevent any prior decomposition of the precursor before
47 reaching the reactor chamber. The stock precursor solution consisted of tungsten hexacarbonyl
48 (0.6 g, 11.4 mM), dissolved in a mixture of acetone (100 ml) and methanol (50 ml). This stock
49
50
51
52
53
54
55
56
57
58
59
60

1
2
3 solution was sonicated for 10 minutes to dissolve the solid (VWR ultra-sonic cleaner, 30 W, 45
4 kHz) and stored in the dark. A set volume was used for each deposition, which was aerosolized
5 using an ultrasonic humidifier (2 MHz, Liquifog – Johnson Matthey) and passed over the heated
6 FTO substrate using an N₂ carrier gas (99.99 %, BOC) controlled by a mass flow controller
7 (MFC, Brooks). For the growth of flat WO₃ materials, the reaction was conducted at 325 °C with
8 a carrier gas flow rate of 500 sccm, transferring volumes of 1.0, 2.5, 5.0 or 10 ml. For the growth
9 of nano-needle WO₃ structures, the reaction was conducted at 375 °C with a carrier gas flow rate
10 of 300 sccm, transferring volumes of 2.5, 5.0, 10 or 20 ml. Three groups of samples were
11 synthesized: (i) flat WO₃ materials, (ii) nano-needle WO₃ structures and (iii) a combination of
12 flat WO₃ followed by nano-needle WO₃ structures grown on top. After the precursor solution
13 had been completely transferred, the material was cooled to room temperature under a carrier gas
14 flow of N₂. All deposited materials were post heat-treated at 500 °C in air for 12 hrs.

15
16
17
18
19
20
21
22
23
24
25
26
27
28
29
30
31
32 **Physical Characterization:** The surface morphology was investigated by scanning electron
33 microscopy (SEM) on a JOEL-6301F field emission instrument. X-ray diffraction (XRD)
34 patterns were measured with a modified Bruker-Axs D8 diffractometer with parallel beam optics
35 equipped with a PSD LinxEye silicon strip detector. The instrument uses a Cu source for X-ray
36 generation (V = 40 kV, I = 30 mA) with Cu K_{α1} (λ = 1.54056 Å) and Cu K_{α2} radiation (λ =
37 1.54439 Å) emitted with an intensity ratio of 2: 1. The incident beam was kept at 1° and the
38 angular range of the patterns collected between 20 ≤ 2θ° ≤ 60 with a step size of 0.05°. A Le
39 Bail model was fit to each diffraction pattern using GSAS-EXPGUI software.³⁵ High-resolution
40 transmission electron microscopy (HR-TEM) images were obtained using a high resolution TEM
41 Jeol 2100 with a LaB₆ source operating at an acceleration voltage of 200 kV. Micrographs were
42 recorded on a Gatan Orius Charge-coupled device (CCD). The films were scratched off the
43
44
45
46
47
48
49
50
51
52
53
54
55
56
57
58
59
60

1
2
3 quartz substrate using a scalpel, suspended in n-hexane, sonicated and then drop-casted onto a
4
5 400 Cu mesh lacy carbon grid (Agar Scientific Ltd.) for analysis. X-ray photoelectron
6
7 spectroscopy (XPS) was carried out using a Thermo K-Alpha spectrometer with monochromated
8
9 Al K_{α} radiation. Survey scans were collected over the 0 – 1400 eV binding energy range with 1
10
11 eV resolution and a pass energy of 200 eV. Higher resolution scans (0.1 eV) encompassing the
12
13 principal peaks of C (1s), O (1s), F (1s), Si (2p), W (4f) and the valence band region (-5 to 15
14
15 eV) were also collected at a pass energy of 50 eV. Sub-surface layers were investigated by Ar-
16
17 ion sputtering. Peaks were modeled using CasaXPS.³⁶ Peak positions were calibrated to
18
19 adventitious carbon (284.5 eV) and peak areas were adjusted using the appropriate sensitivity
20
21 factors to determine the population fraction of each state.³⁷ UV-visible transmittance and
22
23 reflectance spectra were recorded over the 250 – 1100 nm range using a Helios double beam
24
25 instrument equipped with an integrating sphere. Brunauer-Emmett-Teller (BET) surface area
26
27 analysis (N_2 adsorption) was obtained using a TriStar II PLUS system (Micromeritics,
28
29 Hertfordshire, UK) and processed using MicroActive™ software. Nanopowder was collected
30
31 from CVD-produced films using a scalpel. 5 mg of the nanopowder was wrapped in tin foil and
32
33 degassed overnight at 150 °C under flowing nitrogen gas. The relative pressure (P/P_0) was
34
35 measured over the range 0.05 to 0.30 at 10 discrete points.
36
37
38
39
40
41
42

43 **Photoelectrochemistry:** All photoelectrochemical analyses were carried out in a home-made
44
45 PEEK cell with quartz windows. The electrolyte was 0.5 M H_2SO_4 in Milli-Q-water (Millipore
46
47 Corp., 18.2 M Ω .cm at 25 °C) (pH = 0.56). A three-electrode configuration was used, with a Pt
48
49 mesh counter electrode, a Ag/AgCl/saturated-KCl reference electrode (0.197 V_{NHE} at 25 °C;
50
51 Metrohm) and the WO_3 photoanode as the working electrode.
52
53
54
55
56
57
58
59
60

On measuring current-voltage curves, a 365 nm LED light source was used (LZ1-10U600, LedEngin. Inc.) to photo-excite the materials. The light intensity was measured using an optical power meter (PM 100, Thorlabs) coupled with a power sensor (S120UV, Thorlabs). An Autolab potentiostat (PGSTAT12 with an FRA2 module) was used to apply voltage and measure currents. The applied voltages are reported vs the reversible hydrogen electrode (V_{RHE}), converted using the Nernst equation:

$$V_{RHE} = V_{Ag/AgCl} + 0.0591 \times pH + V_{Ag/AgCl}^o \quad (\text{Equation 1})$$

The incident photon to current efficiency (IPCE) was measured using an ozone-free xenon lamp (75 W, Hamamatsu) coupled with a monochromator (OBB-2001, Photon Technology International). The IPCE was calculated using the following equation:

$$IPCE (\%) = \frac{I_{ph} \times 1239.8}{P_{mono} \times \lambda} \times 100 \quad (\text{Equation 2})$$

where I_{ph} ($\text{mA} \cdot \text{cm}^{-2}$) is the photocurrent, 1239.8 ($\text{eV} \cdot \text{nm}$) is a multiplication of Planck's constant with the speed of light, P_{mono} ($\text{mW} \cdot \text{cm}^{-2}$) is the power and λ (nm) is the wavelength of the monochromated light.

The solar water splitting activity of the WO_3 photoanodes were predicted from IPCE measurements. This solar predicted photocurrent (SPP) was determined by multiplying the IPCE with the AM1.5 solar spectrum, and then converting this into a current:

$$SPP (\text{mA} \cdot \text{cm}^{-2}) = \int_{3000 \text{ nm}}^{280 \text{ nm}} IPCE \times AM1.5 (\text{photon} \cdot \text{cm}^{-2}) \times 1000 / 1C \quad (\text{Equation 3})$$

1
2
3 where $1C$ is 6.241×10^{18} electrons per second. The solar-to-hydrogen efficiency (η) could be
4
5
6 calculated from this solar predicted photocurrent:

$$\eta (\%) = \frac{SPP (mA.cm^{-2}) \times (1.23V - V_{app})}{P_{in} (mW.cm^{-2})} \times 100 \quad (\text{Equation 4})$$

7
8
9
10
11
12 where V_{app} is the voltage applied when measuring the SPP and P_{in} is the power of AM1.5
13
14 solar light (100 mW.cm^{-2}).

15
16
17 Faradaic efficiency measurements were carried out in a gas tight, three electrode
18
19 electrochemical cell. The sample was held at 1.23 V_{RHE} in $0.5 \text{ M H}_2\text{SO}_4$ ($\text{pH} = 0.56$) in the
20
21 presence of a UV light source (365 nm LED , $\sim 30 \text{ mW.cm}^{-2}$). The oxygen evolution was analyzed
22
23 with a gas-phase Clark-type oxygen electrode (Unisense Ox-N needle microsensor). At the end
24
25 of the experiment the cell was calibrated by adding known amounts of air. The Faradaic
26
27 efficiency (FE) was estimated using the following equation:

$$FE (\%) = \frac{\text{real moles of } O_2}{\text{theoretical moles of } O_2} \times 100 \quad (\text{Equation 5})$$

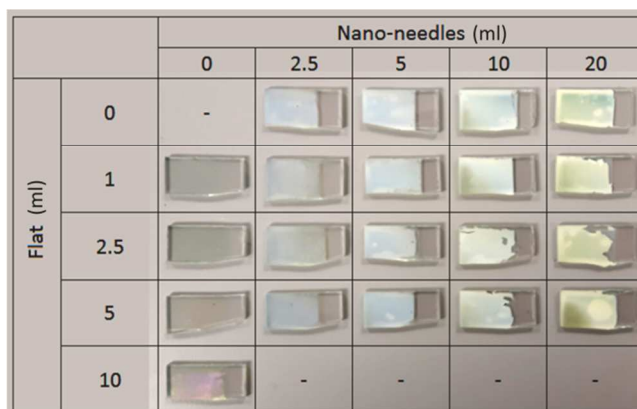
28
29
30
31
32
33
34
35
36 where real moles of O_2 were quantified using a Clark electrode in the gas phase and the
37
38 theoretical moles of O_2 was the amount of oxygen that the system could produce, assuming a
39
40 100% Faradaic conversion efficiency. The latter was estimated from photocurrent measurements,
41
42 which can be converted into mol of O_2 taking into account the Faraday constant (96485 C / mole
43
44 of electrons) and the requirement of 4 electrons to produce 1 mol of oxygen.
45
46
47

48 **RESULTS AND DISCUSSION**

49
50
51
52 WO_3 photoanodes were grown using an aerosol-assisted chemical vapor deposition (AACVD)
53
54 method. Those grown at $325 \text{ }^\circ\text{C}$ were flat, smooth and well adhered to the FTO substrate. Those
55
56 grown at $375 \text{ }^\circ\text{C}$ appeared hazy and were less well adhered to the FTO substrate (they did not
57
58
59
60

1
2
3 pass the Scotch Tape test). Upon inspection by scanning electron microscopy (SEM), materials
4
5 grown at 325 °C were flat dense structures, whereas those grown at 375 °C were composed of
6
7 nano-needle structures primarily aligned perpendicular to the substrate. Both sets of as-deposited
8
9 materials were initially blue in color, and turned pale yellow after their heat treatment at 500 °C
10
11 in air.
12
13

14
15 In order to find a sample of optimum performance, a series of WO₃ photoanodes were grown
16
17 in a systematic manner – fixing the volume of precursor transferred in each deposition. Three
18
19 types of structure were grown: (i) flat, (ii) nano-needle or (iii) flat with nano-needles grown on
20
21 top. For the purpose of brevity, we will refer to each sample for the remainder of this manuscript
22
23 using a simple code system. First, the type of deposition is stated using a letter, where “F”
24
25 represents flat structures and “NN” represents nano-needle structures. The letter is then followed
26
27 by the approximate thickness as measured by side-on SEM imaging. For dual layers, the two
28
29 types of deposition are comma separated. For example, a WO₃ photoanode grown with 5 ml of
30
31 precursor solution at 325 °C and then subsequently 10 ml of precursor solution at 375 °C is
32
33 called: F ~500 nm, NN ~4.6 μm. A photograph of the WO₃ photoanodes studied herein is shown
34
35 in Figure 1.
36
37
38
39
40
41
42
43



1
2
3 **Figure 1.** A photograph of the WO₃ photoanodes studied herein, positioned in a table that shows
4 the precursor volumes transferred during their synthesis to grow flat WO₃ and/or nano-needle
5 structured WO₃ on top. Flat WO₃ was grown at 325 °C and nano-needle structured WO₃ was
6 grown at 375 °C.
7
8
9
10
11

12
13
14 Surface topographies were investigated by SEM. Micrographs for select samples are shown in
15 Figure 2. One example is shown for a flat structure, F ~800 nm, which was composed of rounded
16 particles approximately 100 nm in diameter. Film thickness was measured by looking at the
17 materials side-on, which increased from ~200 to ~800 nm for flat samples (Table S1). The
18 topography for one example of a nano-needle structure (with no flat layer grown beneath), NN
19 ~4.2 μm, is also shown in Figure 2. Nano-needles were around 4 μm long and were roughly 100
20 nm in diameter. In general, these needles were aligned vertically from the substrate. The effect of
21 increasing precursor volume is also shown for a series of flat samples (F ~300 nm) with nano-
22 needles grown on top (N ~2.3, 4.6 and 6.2 μm). As the volume of precursor transfer increased,
23 both the length and width of the nano-needles also increased. At higher deposition volumes, the
24 tips of the nano-needles began to merge. An example side on SEM image for sample F ~300 nm,
25 NN ~4.6 μm is shown in Figure S2. Needles were primarily aligned perpendicular to the
26 substrate, and stacked on top of each other to some degree. It is worthy of note that the complex
27 nano-needle structures observed herein are not so readily formed in other photoelectrode
28 materials, and often require multiple steps or expensive patterning methods such as lithography
29 to achieve similar nanostructure.²⁹
30
31
32
33
34
35
36
37
38
39
40
41
42
43
44
45
46
47
48
49
50
51
52
53
54
55
56
57
58
59
60

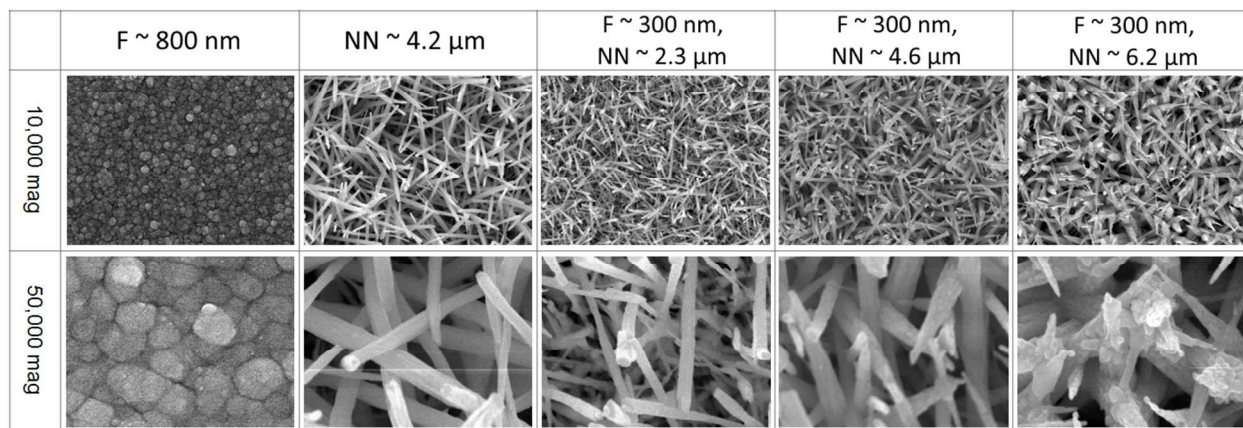


Figure 2. Top down SEM images of select WO_3 photoanodes at 10,000 and 50,000 magnification. The width of images taken at 10,000 and 50,000 magnifications are 7.0 and 1.4 μm respectively.

X-ray diffraction (Figure 3) showed that all WO_3 photoanodes produced herein were phase pure and adopted the monoclinic $\gamma\text{-WO}_3$ structure ($P2_1/n$, $a = 7.30084(7)$, $b = 7.53889(7)$, $c = 7.68962(7)$ Å, $\beta = 90.892(1)^\circ$).³⁸ In thinner films, peaks corresponding to the FTO substrate were also observed. A Le Bail model was fit to each diffraction pattern. All WO_3 photoanodes produced herein possessed unit cells marginally larger than a powder standard (~0.4 to 1.0 % expansion), albeit with no clear correlation (Table S1). However, there were other discernible relationships. For instance, average crystal size partly increased with the volume of precursor transferred. More striking were the changes in preferred growth, where the tendency to grow in the (002) direction also increased with precursor volume transferred in flat dense structures (Figure S3). However, for nano-needle structures, the tendency to grow in the (002) direction was consistently high.

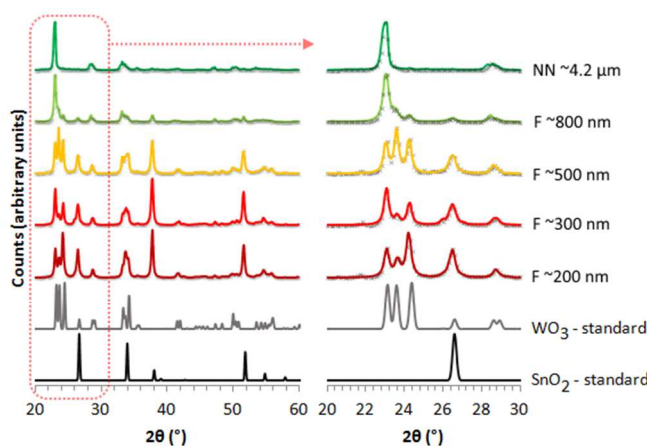


Figure 3. XRD patterns of select samples (cross-hairs) plot alongside their Le Bail model (solid colored lines). The right graph shows a close-up of the region where the largest changes in preferred growth were observed.

The physical properties of the nano-needle structures were further investigated using high-resolution transmission electron microscopy (HR-TEM). The average nano-needle length increased with precursor volume transferred (Figure S4). For the series of nano-needles grown on F ~300 nm, average nano-needle length increased from ~0.7 to ~2.5 μm . These lengths were substantially shorter than the film thicknesses observed by side-on SEM imaging (Table S1). This was because needles grew on top of one another, to some extent, as they grew from the substrate beneath. The needles were highly ordered and showed a strong tendency to grow in the (002) direction (Figure 4). The surface area of a nano-needle sample (F ~300 nm, NN ~4.6 μm) was measured using BET analysis ($\sim 20 \pm 10 \text{ m}^2 \cdot \text{g}^{-1}$), which corresponded to a surface area of around 100 cm^2 per projected area of 1 cm^2 .

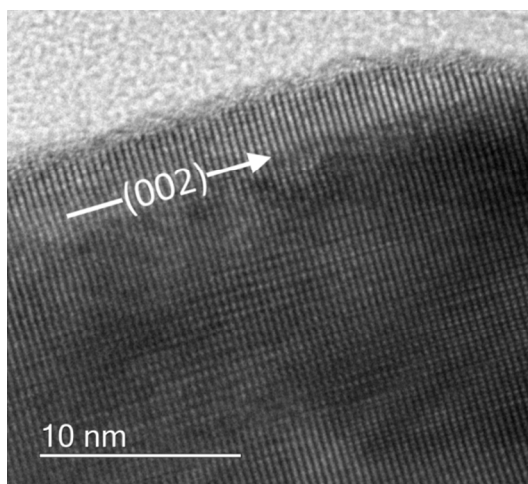


Figure 4. HR-TEM image of the edge of a nano-needle ($F \sim 300$ nm, $NN \sim 4.6$ μm). The spacing between the highly ordered rows of atoms correlates to the d-spacing found in the (002) plane of monoclinic WO_3 (~ 3.86 \AA).

X-ray photoelectron spectroscopy (XPS) was used to study the oxidation states and impurity levels for a number of WO_3 samples. Analysis of the W 4f environment showed no measurable presence of W^{5+} states, and solely the W^{6+} environment, with binding energies similar to reference values (Figure S5a).³⁹ Although not discernible in the W 4f region, W^{5+} states were observed at low binding energies (at ~ 0 eV), albeit in low concentration ($\text{W}^{5+} : \text{W}^{6+} \sim 1 : 2000$). Analysis of this W 5d cross-section revealed a W^{5+} concentration of around $1 \times 10^{19} \text{ cm}^{-3}$. No impurities were observed, with the exception of carbon, which may have been a result of the incomplete decomposition of the $\text{W}(\text{CO})_6$ precursor. Samples were sputtered to probe carbon impurity levels in the bulk (Figure S5b). Nano-needle structures showed little or no presence of carbon in the bulk after 60 s of sputtering. However, flat structures showed carbon impurities deeper into the bulk. In the thinnest sample ($F \sim 200$ nm thick), the carbon impurity level did not reach zero (with respect to surface carbon levels) after 1200 s of sputtering. As film thickness increased, a zero carbon impurity level was reached more quickly, where the thickest flat sample

1
2
3 (F ~800 nm thick) showed no bulk carbon impurities after 300 s of sputtering. Valence band
4
5
6 energy regions were also investigated (Figure S5c). The edge of each valence region was
7
8 extrapolated to the energy axis to determine the energy of the valence band maximum. These
9
10 energies are shown on a band energy diagram, where the energy level is relative to the Fermi
11
12 level of each material, set at zero (Figure S5d). In general, nano-needles possessed less positive
13
14 valence band energies. Also, in flat materials, the valence band energy was less positive in
15
16 thicker films. Physical characterizations showed that there were only two significant differences
17
18 between thin flat films and thicker flat films/ nano-needle structures: (i) the degree of preferred
19
20 growth in the (002) crystal plane and (ii) the carbon impurity level. The observed differences in
21
22 valence band energy may be associated with either physical property.
23
24
25
26

27 The optical properties of the WO₃ photoanodes were assessed using UV-visible spectroscopy
28
29 (Figure 5a). Flat WO₃ structures showed a high degree of transmission in the visible and near
30
31 infrared. Nano-needle structures became increasingly scattering in this region with increasing
32
33 nano-needle length. Moreover, as the needles increased in length, an increasingly red-shifted
34
35 band edge was observed. This increased from ~320 nm in F ~200 nm (no nano-needles present)
36
37 to ~420 nm in F ~300 nm, NN ~6.2 μm. Optical bandgaps were determined from Tauc plots⁴⁰
38
39 (Figure S6). A wide range of optical bandgaps were observed, ranging from ~3.0 eV in sample F
40
41 ~200 nm to ~2.6 eV in sample F ~300 nm, NN ~6.2 μm (Figure 5b). As all of the WO₃
42
43 photoelectrodes adopted the same crystal structure (monoclinic γ-WO₃) and showed similar
44
45 lattice and crystallite sizes, the observed differences in bandgap energy may be due to changes in
46
47 carbon impurity levels, preferential crystal growth or nano-needle length.
48
49
50
51
52
53
54
55
56
57
58
59
60

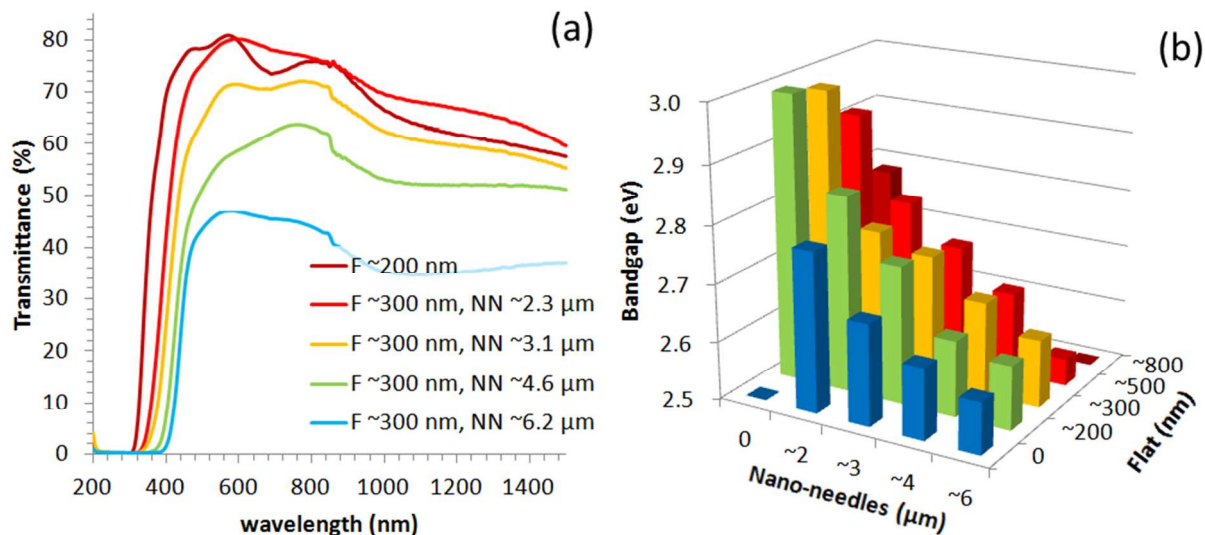


Figure 5. (a) UV-visible spectroscopy showing the transmission of light for select WO₃ samples and (b) a 3D bar chart showing the optical bandgap of all WO₃ samples made herein – derived from Tauc plots.

The water oxidation function of the WO₃ photoanodes was assessed photoelectrochemically. Current-voltage curves were measured by sweeping the voltage from 0.45 V_{RHE} to 2.45 V_{RHE} in the dark and under the action of light (Figure 6). In the dark, electrocatalytic water oxidation was observed from ~2.0 V_{RHE} and above in both flat and nano-needle structures. This was due to the thermodynamic requirement for water oxidation to be surpassed (1.23 V_{RHE}) plus the additional over-potential, which is typically quite high for this kinetically challenging process (*ca.* 0.4 V and above).⁴¹ In flat dense structures, photocatalytic currents decreased when film thickness increased (Figure 6a). In nano-needle structures, comparatively higher photocatalytic currents were observed (Figure 6b), typically five times higher than what was observed in flat materials. Although the onset potentials for photocatalytic oxidation were similar in both flat and nano-needle structures (~0.5 V_{RHE}), the photocurrent increased more steeply in nano-needles

structures; reaching a plateau from almost 0.8 V_{RHE} . From $\sim 2.2 V_{\text{RHE}}$, electrocatalytic oxidation dominated and photocatalysis was not observed.

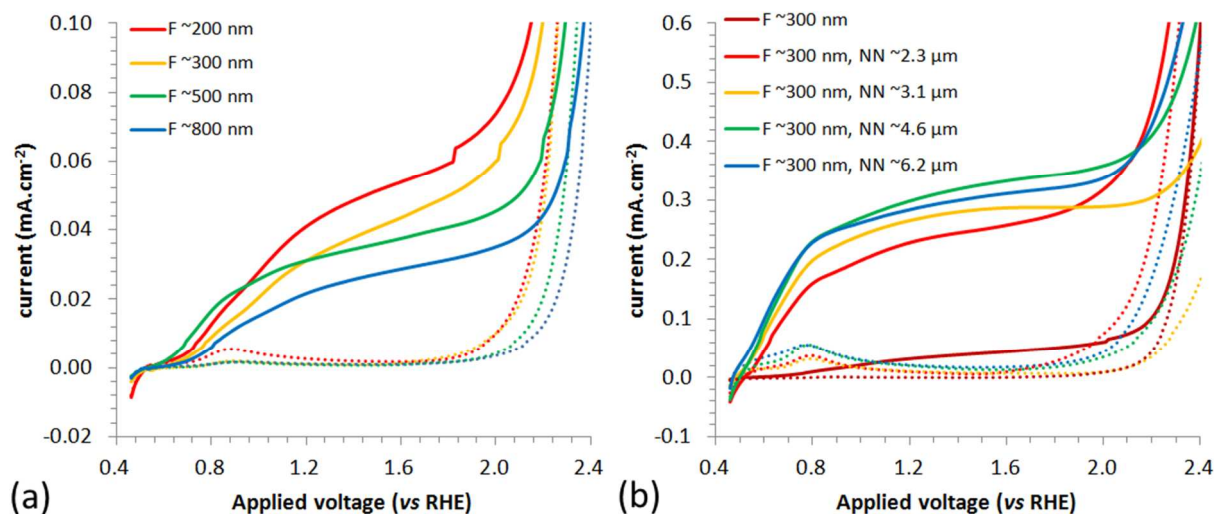


Figure 6. Current-voltage curves of (a) a series of flat WO₃ photoanodes and (b) a series of nano-needle photoanodes with constant flat layer thickness beneath. Samples were measured in the dark (dashed lines) and under the action of light (solid lines; 365 nm LED – 4.2 mW.cm⁻²). The voltage was swept from cathodic to anodic potentials (0.45 – 2.45 V_{RHE}) at a rate of 50 mV.s⁻¹ in 0.5 M H₂SO₄ (pH = 0.56). Samples were irradiated at the semiconductor-electrolyte interface.

The incident photon-to-current efficiency (IPCE) was measured at a range of wavelengths for each sample, holding the photoanode at 1.23 V_{RHE} (the thermodynamic potential for water oxidation). Samples were irradiated from either the front (semiconductor-electrolyte interface) or back (electrode-electrolyte interface). When considering arrangements within a tandem cell device, it is particularly useful to examine the photocatalytic performance of a photoelectrode under both front and back irradiation (Figure S7). For flat materials, the quantum efficiency was in the range 20 to 30 % in the UVC (range 250 – 300 nm) upon front irradiation, which steadily declined to 0 % in the near visible (450 nm, Figure S8a). When irradiating from the back, the

quantum efficiency was substantially lower in the UVC region (Figure S8b). This was due to the unfavorable absorption of light by the FTO electrode ($E_{bg} \sim 3.6$ eV), which shielded the WO_3 layer from UVC irradiation. However, comparing results from front and back irradiation, similar efficiencies were observed from 350 nm and above. In flat WO_3 materials, IPCEs decreased as film thickness increased.

In nano-needle structures, quantum efficiencies in the UVC region were similar to flat materials, in the range ~ 25 to 30 % (Figure 7a). In stark contrast to flat materials, the quantum efficiency increased on movement into the UVA region (range 325 – 375 nm), with efficiencies in the range ~ 30 to 45 %. In general, thicker nano-needle structures possessed higher levels of visible light activity. The quantum efficiency in the UVC was substantially reduced when irradiating from the back, due to unfavorable light absorption by the FTO substrate (Figure 7b).

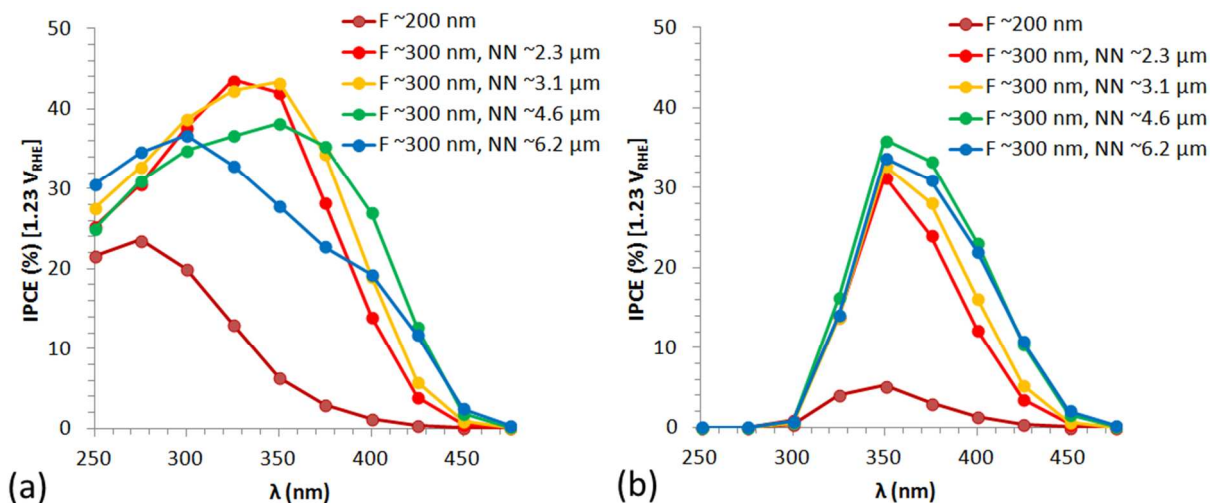


Figure 7. Incident photon-to-current efficiencies (IPCE) for select WO_3 photoanodes. Samples were measured at 1.23 V_{RHE} in 0.5 M H_2SO_4 (pH = 0.56) under (a) front [semiconductor-electrolyte interface] and (b) back [electrode-electrolyte interface] illumination. Each wavelength was selected using a monochromator using a Xe light source (~ 10 $mW \cdot cm^{-2}$ over the range of wavelengths studied).

To predict which WO_3 photoanode would be best suited for solar water splitting applications, we determined a solar predicted photocurrent (SPP) for the 20 unique samples studied herein. This was determined by multiplying the IPCE with the AM1.5 solar spectrum using Equation 3, shown graphically in Figure 8 for sample F ~ 300 nm, NN ~ 4.6 μm .

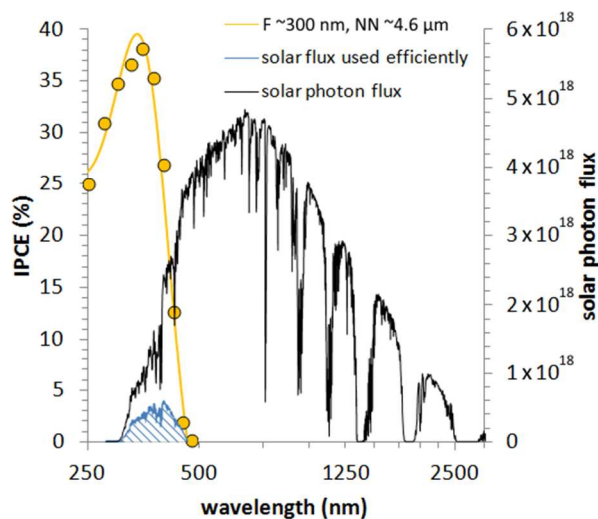


Figure 8. The theoretical portion of solar light that would be converted into photocurrent by sample F ~ 300 nm, NN ~ 4.6 μm when held at $1.23 V_{\text{RHE}}$.

As solar light contains few UVC photons, the relatively high quantum efficiency seen in this region is of little benefit for solar applications. However, materials that possessed higher efficiencies in the UVA and near visible would be of greater benefit. Therefore, the nano-needle structures, which showed higher IPCEs in the near-visible, showed higher solar predicted photocurrents compared with flat structures (Figure 9).

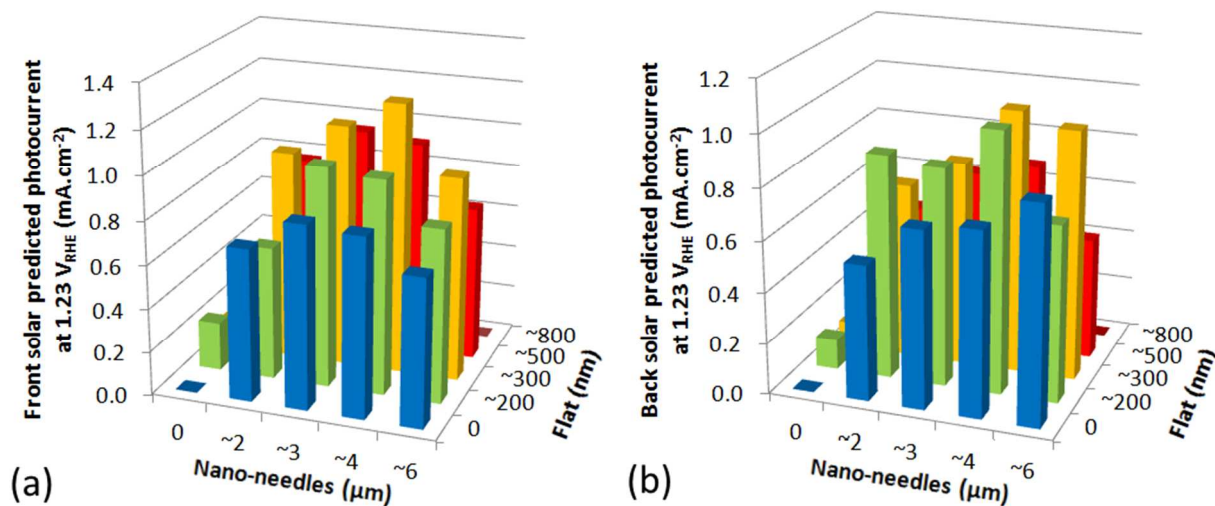


Figure 9. Solar predicted photocurrents for all WO₃ photoanodes for both (a) front and (b) back illumination. These photocurrents were predicted from IPCE measurements conducted at 1.23 V_{RHE} in 0.5 M H₂SO₄ (pH = 0.56) using Equation 3.

In general, SPPs showed that WO₃ nano-needles were *ca* 3 to 5 times more active than their flat counterparts. However, materials composed of both a flat “seed” layer with nano-needles grown on top were notably more active than needles alone. The authors attribute this to the greater density of nano-needles formed when a seed layer was present (Figure 2). The SPPs were calculated for both cases of front and back irradiation. Generally, back irradiation resulted in slightly lower SPPs (because of unfavorable light absorption by the FTO layer). Looking at the SPPs for front irradiation (Figure 9a), a clear trend to the best performing sample was observed; F ~300 nm, NN ~4.6 μm. Looking at the SPPs for back irradiation (Figure 9b), a trend was less clear. What could be said was that nano-needle structures with flat “seed” layers between ~200 – 300 nm in thickness (F ~200 – 300 nm) were the most active. Although there was no clear trend in the case of back irradiation, the best performing sample was again sample F ~300 nm, NN ~4.6 μm.

The solar predicted photocurrents observed herein ($0.06 - 1.24 \text{ mA}\cdot\text{cm}^{-2}$) are now compared with the literature (Table 1). Lee *et al.* hydrothermally grew monoclinic WO_3 nanocrystals, and doctor-bladed them to form a mesoporous photoelectrode.⁴² Under AM1.5 solar simulated light, they observed photocurrents of $\sim 0.6 \text{ mA}\cdot\text{cm}^{-2}$ at $\sim 1.23 \text{ V}_{\text{RHE}}$ and reported an IPCE of $\sim 25 \%$ at 340 nm. Grimes *et al.* solvothermally grew WO_3 nanowire structures, which showed IPCEs of $\sim 60 \%$ at 400 nm and photocurrents of $\sim 1.4 \text{ mA}\cdot\text{cm}^{-2}$ when held at $1.23 \text{ V}_{\text{RHE}}$ and exposed to AM1.5 solar simulated light.⁴³ Fàbrega *et al.* grew WO_3 nano-needle structures using a pulsed laser deposition process, which showed photocurrents of $2.4 \text{ mA}\cdot\text{cm}^{-2}$ at $1.23 \text{ V}_{\text{RHE}}$ under AM1.5 solar simulated light.¹⁸ WO_3 photoanodes have also previously been grown using CVD processes. Sunkara *et al.* grew WO_3 nano-needle structures at reduced pressure ($\sim 100 \text{ Pa}$) using a hot-wire technique.³¹ These photoanodes showed photocurrents of $\sim 1.0 \text{ mA}\cdot\text{cm}^{-2}$ at $1.23 \text{ V}_{\text{RHE}}$ under AM1.5 solar simulated light. Rao *et al.* also grew WO_3 nano-needle structures by CVD, this time at atmospheric pressure.¹⁵ In their case, a seed layer grown using wet-chemical methods was required to promote dense and uniform growth of nano-needles. Under AM1.5 solar simulated light these photoanodes reached photocurrents of $\sim 1.6 \text{ mA}\cdot\text{cm}^{-2}$ at $\sim 1.3 \text{ V}$ vs a Pt counter electrode using a 2 electrode configuration.

Table 1. Summary of the synthesis, microstructure and photocatalytic water oxidation activity for various WO_3 photoanodes reported in the literature.

Synthesis ^[a]	Microstructure	Photocatalytic activity		Reference
		Photocurrent ^[b]	IPCE	
Hydrothermal	Mesoporous film of interconnected WO_3 nanospheres (each $\sim 50 \text{ nm}$ in diameter, forming a film $\sim 9 \mu\text{m}$ thick)	$\sim 0.6 \text{ mA}\cdot\text{cm}^{-2}$	$\sim 25 \%$, 340 nm	Lee <i>et al.</i> ⁴²

Spin-coating + Solvothermal	Array of vertically aligned nanoflakes (~20 – 30 nm thick and ~5.6 μm wide)	~1.4 mA.cm ⁻²	~60 %, 400 nm	Grimes <i>et al.</i> ⁴³
Pulsed laser deposition (~13 Pa)	Array of closely-packed, vertically aligned nano-needles (~17.6 μm long)	~2.4 mA.cm ⁻²	~50 %, 410 nm	Fàbrega <i>et al.</i> ¹⁸
CVD (~100 Pa)	Array of vertically aligned nano-needles (~40 – 70 nm in diameter and ~2 – 3 μm long)	~1.0 mA.cm ⁻²	~35 %, 425 nm	Sunkara <i>et al.</i> ³¹
Spin-coating + CVD	Array of vertically aligned hollow nano-needles (~15 μm thick)	~1.6 mA.cm ⁻² _[c]	-	Rao <i>et al.</i> ¹⁵
CVD	Flat WO ₃ films (~200 – 800 nm thick)	~0.1 – 0.2 mA.cm ⁻² [d]	~2 %, 400 nm	herein
CVD	Array of vertically aligned nano-needles (~100 nm in diameter and ~2 – 6 μm long)	~0.6 – 1.24 mA.cm ⁻² [d]	~27 %, 400 nm	herein

[a] synthesis conducted at atmospheric pressure unless specified; [b] photocurrent at 1 sun irradiance (AM1.5 solar simulated light, 100 mW.cm⁻²) and a applied potential of 1.23VRHE; [c] photocurrent achieved at ~1.3 V vs a Pt counter electrode in a 2 electrode configuration; [d] solar predicted photocurrents (see Equation 3).

Photon penetration depths (Figure 10) were determined from a flat sample of known thickness (F ~300 nm thick). Absorption coefficients were calculated from transmission data:

$$\alpha \text{ (cm}^{-1}\text{)} = -\frac{\ln T}{l \text{ (cm)}} \quad \text{(Equation 6a)}$$

where T is the fraction of transmitted light and l is material thickness. The penetration depth was then solved analytically, where for a given fraction of light absorbed, δ, the exponent y was determined:

$$\delta = 1 - \left(\frac{1}{e^y}\right) \quad \text{(Equation 6b)}$$

where y/α is the photon penetration depth. Using the photon penetration depth, differences in light conversion behaviour between materials of nano-needle and flat structure were rationalized. This was done keeping in mind the respective electron ($\sim 7 \mu\text{m}$)⁴⁴ and hole diffusion lengths ($\sim 150 \text{ nm}$)⁴⁵ of WO_3 .

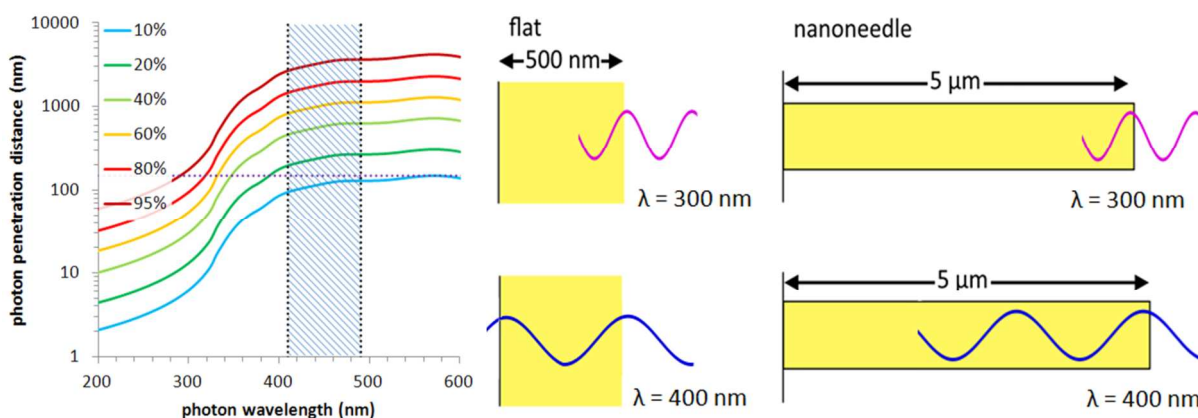


Figure 10. (left) Photon penetration depth for a range of light fractions absorbed. The purple dashed horizontal line represents the hole diffusion length in WO_3 ($\sim 150 \text{ nm}$). The blue dashed area represents the range of bandgaps found in the WO_3 photoanodes. (right) Visual examples showing where light of different wavelengths are absorbed in WO_3 materials of flat or needle structure.

Considering the case of front irradiation (semiconductor-electrolyte interface) in a flat material, 95 % of UV light (range 250 – 300 nm) would be absorbed within the first 150 nm (Figure 10). As such, holes would be capable of diffusing back to the semiconductor-electrolyte interface and taking part in photocatalytic reactions. However, in the case of near-visible light (400 nm), less than 20 % of light would be absorbed within the first 150 nm, meaning a large portion of holes would be incapable of diffusing back to the semiconductor-electrolyte interface. This was reflected in the IPCE spectra of flat materials in that efficiencies were higher in the UVC region (range 250 – 300 nm, $\sim 20 \%$) compared with the near-visible region (400 nm, ~ 2

1
2
3
4
5
6
7
8
9
10
11
12
13
14
15
16
17
18
19
20
21
22
23
24
25
26
27
28
29
30
31
32
33
34
35
36
37
38
39
40
41
42
43
44
45
46
47
48
49
50
51
52
53
54
55
56
57
58
59
60

%). Now if we consider the case of front irradiation of a nano-needle structured material, there is no requirement for holes to diffuse back to the material surface, as the needles are exposed to water on all fronts. As needles were ~ 100 nm wide, holes would be able to diffuse to the semiconductor-electrolyte interface wherever generated inside the needle. In addition to this, thicker nano-needle structures (> 4 μm) were sufficiently long to facilitate complete light absorption in the near-visible range. This was reflected in the IPCE spectra of nano-needle structures, where efficiencies were consistently high across the UVC and near-visible regions (range 250 - 400 nm, $\sim 20 - 40$ %). However, as the thickness of the nano-needle structures grown herein increased from ~ 4 to ~ 6 μm , a small decrease in activity was observed, which coincided with an approach to the electron diffusion length limit.

The stability of the best performing sample, F ~ 300 nm, NN ~ 4.6 μm , was evaluated over a period of 4 hours (Figure S9). Simulating conditions of device operation, the material was held at a positive potential for several hours under the action of chopped UV light. For comparison, a flat structure was also examined, F ~ 500 nm. Photocurrents were superior in the nano-needle structured material, but were initially less stable, dropping by ~ 20 % in the first 30 minutes. After 210 minutes, the photocurrent stabilized, but was ~ 40 % lower than the initial value. In the flat structured material, the photocurrent marginally increased before stabilizing, and showed no loss in performance over the testing period. The loss in performance in the nano-needle structures produced herein was attributed to the poor adherence of needles to the FTO substrate, which flaked off during testing. This was more prominent in photoelectrodes with thicker nano-needle stacks (NN > 4 μm) and occurred less so in thinner nano-needle structures (NN < 3 μm). Recent studies have shown that the stability of nanostructured WO_3 photoanodes can be increased when co-catalysts such as nickel borate⁴⁶ and iron oxy-hydroxide⁴⁷ are grown at the

1
2
3 surface; where these co-catalysts also improve the Faradaic efficiency of water oxidation. Choi
4
5 *et al.* studied a range of electrolytes and found that the use of acetate based electrolytes
6
7 improved photostability substantially compared with phosphate, perchlorate and chloride based
8
9 electrolytes.⁴⁸ The Faradaic efficiency of the best performing sample, F ~300 nm, NN ~4.6 μm,
10
11 was also measured, yielding a Faradaic efficiency of ~64 % (Figure S10). Deviations from
12
13 Faradaic unity are common in WO₃ photoelectrodes, and have been attributed to the material's
14
15 deeply oxidizing valence band.⁴⁸ Previous studies of WO₃ photoelectrodes in sulfate solutions
16
17 have shown that water oxidation to di-oxygen competes with sulfate oxidation to persulphate⁵⁰
18
19 and incomplete water oxidation to form peroxy species⁵¹ (which accumulate on the material
20
21 surface and cause a gradual decay in the , also observed herein). A comprehensive study of the
22
23 Faradaic efficiencies of water oxidation for WO₃ photoelectrodes was recently conducted by
24
25 Choi *et al.*⁴⁸ Their studies showed that water oxidation was inhibited in highly acidic solutions,
26
27 where a Faradaic efficiency of 35 % was recorded in pH = 1. In these studies, the Faradaic
28
29 efficiency of water oxidation was almost double that observed by Choi *et al.* for a similarly
30
31 acidic pH. We believe that this enhancement in selectivity may be due to the preferential crystal
32
33 growth of nano-needle structures and is currently the subject of an ongoing study.
34
35
36
37
38
39

40
41 The IPCE of the best performing sample, F ~300 nm, NN ~4.6 μm, was measured at a range of
42
43 applied potentials. This allowed us to create a 3D contour map of efficiency *vs* wavelength and
44
45 applied potential (Figure 11). IPCE decreased almost linearly with applied potential, and
46
47 followed a similar trend to its current-voltage curve (Figure 6b). For a given applied potential,
48
49 the measured IPCE was used to calculate the solar predicted photocurrent (SPP), which in turn
50
51 was used to determine solar-to-hydrogen efficiencies using Equation 4. For a voltage-assisted
52
53
54
55
56
57
58
59
60

water splitting device, solar-to-hydrogen efficiencies peaked at 0.9 V_{RHE} for both front ($\eta = 0.25$ %) and back ($\eta = 0.21$ %) irradiation (Figure S11).

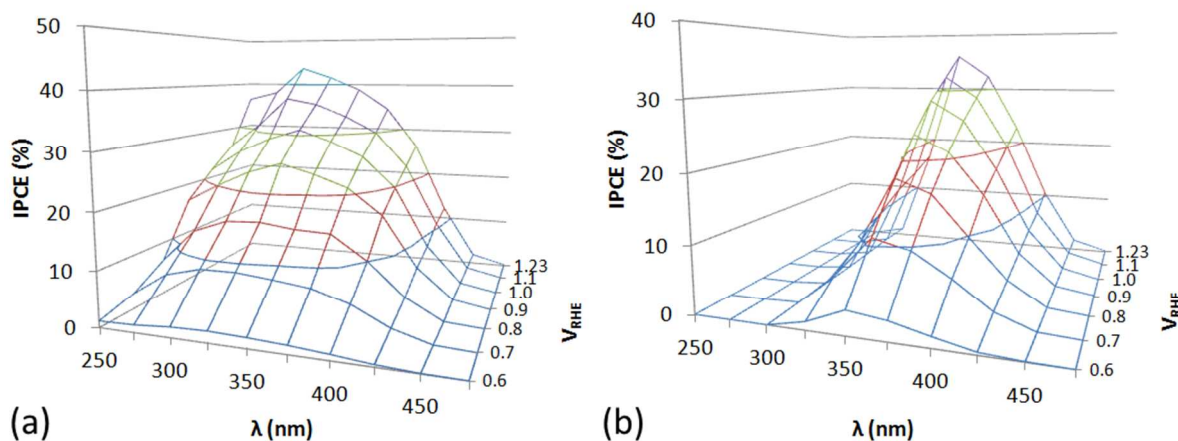


Figure 11. The change in incident photon-to-current efficiency (IPCE) at various applied potentials in 0.5 M H_2SO_4 (pH = 0.56) for the best performing sample, F \sim 300 nm, NN \sim 4.6 μm . The sample was measured under (a) front [semiconductor-electrolyte interface] and (b) back [electrode-electrolyte interface] illumination. Each wavelength was selected using a monochromator using a Xe light source (\sim 10 $\text{mW}\cdot\text{cm}^{-2}$ over the range of wavelengths studied).

The ability of the best performing WO_3 photoanode produced herein to work in tandem with a solar cell was also assessed. A methyl ammonium lead iodide perovskite solar cell was chosen, as it can provide the high voltage required for WO_3 photoanodes to operate ($V_{\text{oc}} = 0.96$ V, $J_{\text{sc}} = 16.1$ $\text{mA}\cdot\text{cm}^{-2}$, FF = 0.45, efficiency = 7 %). The architecture and synthetic details of how the solar cell was made is described in a previous publication.⁵² As the WO_3 photoanode possesses the wider bandgap, light must be passed through the back of this material first (tandem cell arrangement shown in Figure S7b). Under operating conditions, the solar cell provided 0.85 V of potential. As the solar cell provided 0.85 V of potential, current-matching between the WO_3 photoanode and a Pt electrocatalyst showed that the photoanode would operate at 0.8 V_{RHE}

(Figure S12b). The IPCE of the WO_3 photoanode at 0.8 V_{RHE} under back irradiation was used to determine the solar predicted photocurrent ($\sim 0.6 \text{ mA}\cdot\text{cm}^{-2}$, Figure 12). Similarly, the IPCE of the solar cell, measured through a WO_3 filter, was used to determine the solar predicted current ($\sim 3.5 \text{ mA}\cdot\text{cm}^{-2}$). The tandem cell was limited by the performance of the WO_3 photoanode, as it generated a lower photocurrent than the solar cell. We predict the overall solar-to-hydrogen efficiency of the tandem cell to be $\sim 0.75\%$. Similar work conducted by Kamat *et al.* showed that a tandem cell consisting of a BiVO_4 photoanode coupled with a perovskite solar cell could achieve solar-to-hydrogen efficiencies of $\sim 2.5\%$.⁵³ We attribute their higher performance to the increased solar light absorption of BiVO_4 ($E_{\text{bg}} \sim 2.4 \text{ eV}$) compared with WO_3 ($E_{\text{bg}} \sim 2.7 \text{ eV}$). Similarly, Sivula *et al.* showed that tandem cells consisting of either an $\alpha\text{-Fe}_2\text{O}_3$ or WO_3 photoanode paired with a dye-sensitized solar cell can reach solar-to-hydrogen efficiencies of $\sim 1.2\%$ and $\sim 3.1\%$ respectively.²⁴ We attribute the higher performance of Sivula *et al.*'s WO_3 -based tandem cell to the higher operating voltage of his solar cell ($\sim 1.0 \text{ V}$) and the higher light conversion efficiency of his WO_3 photoanodes, grown using a sol-gel process.

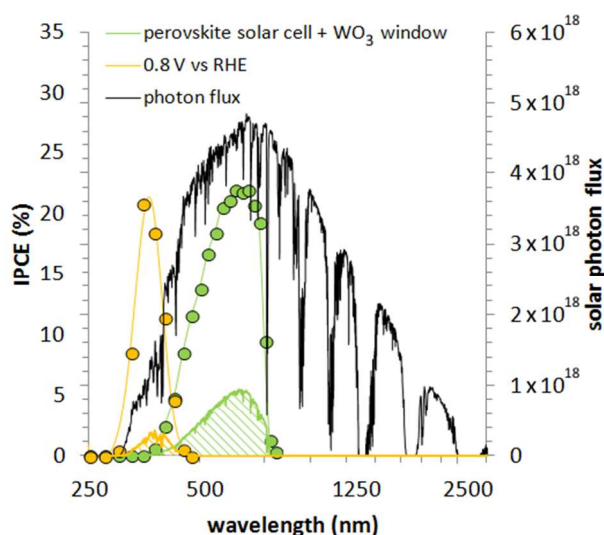


Figure 12. The theoretical solar performance of a tandem cell device consisting of a WO_3 photoanode (sample F $\sim 300 \text{ nm}$, NN $\sim 4.6 \mu\text{m}$, first light absorber) and a perovskite solar cell

1
2
3 (second light absorber). As the solar cell provided 0.85 V of potential, current-matching between
4
5 the WO₃ photoanode and a Pt electrocatalyst showed that the photoanode would operate at 0.8
6
7
8 V_{RHE}.
9

10 11 **CONCLUSIONS**

12
13 In this article, a route to produce WO₃ photoelectrodes is developed using chemical vapor
14
15 deposition at atmospheric pressure – a low-cost technique use widely for the mass-production of
16
17 nanoscale coatings. We believe that this is the first time in which WO₃ photoanodes have been
18
19 entirely fabricated using chemical vapor deposition processes at atmospheric pressure. The
20
21 chosen synthesis method offers a direct, inexpensive and scalable route with promising potential
22
23 for future scale-up. Two growth conditions were investigated, one in which flat and dense WO₃
24
25 structures were grown at 325 °C and the other in which stacked nano-needles were formed at 375
26
27 °C. These two growth conditions, and their combinations, were systematically studied in order to
28
29 determine the conditions for optimal water splitting performance. Photoelectrodes that showed
30
31 the highest efficiencies were composed of a ~300 nm seed layer of flat WO₃ with a ~5 μm thick
32
33 top layer of WO₃ nano-needles. When held at 1.23 V_{RHE}, this material showed incident photon-
34
35 to-current efficiencies of ~40 % in the UV region (from 250 – 375 nm) and a solar predicted
36
37 photocurrent of 1.24 mA.cm⁻² (~25 % of the theoretical maximum). When coupled in tandem
38
39 with a photovoltaic device containing a methyl ammonium lead iodide perovskite absorber, we
40
41 predict a solar-to-hydrogen efficiency of roughly 1 % for a complete unassisted water splitting
42
43 device.
44
45
46
47
48
49
50
51
52
53

54 **AUTHOR INFORMATION**

55 56 **Corresponding Author** 57 58 59 60

*corresponding author; e-mail: a.kafizas@imperial.ac.uk

Author Contributions

The manuscript was written through contributions of all authors. All authors have given approval to the final version of the manuscript.

ACKNOWLEDGMENT

AK would like to thank Imperial College London for a Junior Research Fellowship. LF thanks the EU for a Marie Curie fellowship (658270). YL thanks the China Scholarship Council (CSC File No. 201406370157) for funding, and the UCL Dean's prize for the joint PhD scholarship. CS-V thanks the European Commission FP7 for funding (PCATDES, Grant N.309846). IPP thanks the EPSRC for an M3S CDT (EP/L015862/1). LM and JD thank the EPSRC for funding (EP/M008754/1). Dr. Steve Firth is thanked for his assistance for our HRTEM and SEM studies. Dr. Xiaoe Li is thanked for her assistance with the preparation of the perovskite solar cell.

ABBREVIATIONS

AACVD, aerosol-assisted chemical vapor deposition; CVD, chemical vapor deposition; FE, Faradaic efficiency; HR-TEM, high-resolution transmission electron microscopy; IPCE, incident photon to current efficiency; SEM, scanning electron microscopy; SPP, solar predicted photocurrent; XPS, X-ray photoelectron spectroscopy; XRD, X-ray diffraction.

REFERENCES

- (1) Broecker, W. S. Climatic Change: Are We on the Brink of a Pronounced Global Warming? *Science* (80-.). **1975**, *189*, 460–463.
- (2) Gruber, N. Warming Up, Turning Sour, Losing Breath: Ocean Biogeochemistry under

- 1
2
3 Global Change. *Philos. Trans. A. Math. Phys. Eng. Sci.* **2011**, 369, 1980–1996.
4
5
6
7 (3) Morton, O. Solar Energy: A New Day Dawning? Silicon Valley Sunrise. *Nature* **2006**,
8
9 443, 19–22.
10
11
12 (4) Sovacool, B. K. The Intermittency of Wind, Solar, and Renewable Electricity Generators:
13
14 Technical Barrier or Rhetorical Excuse? *Util. Policy* **2009**, 17, 288–296.
15
16
17
18 (5) Beaudin, M.; Zareipour, H.; Schellenberglobe, A.; Rosehart, W. Energy Storage for
19
20 Mitigating the Variability of Renewable Electricity Sources: An Updated Review. *Energy*
21
22 *Sustain. Dev.* **2010**, 14, 302–314.
23
24
25
26 (6) Tachibana, Y.; Vayssieres, L.; Durrant, J. R. Artificial Photosynthesis for Solar Water-
27
28 Splitting. *Nat. Photonics* **2012**, 6, 511–518.
29
30
31
32 (7) Fujishima, A.; Honda, K. Electrochemical Photolysis of Water at a Semiconductor
33
34 Electrode. *Nature* **1972**, 238, 37–38.
35
36
37
38 (8) Walter, M. G.; Warren, E. L.; Mckone, J. R.; Boettcher, S. W.; Mi, Q.; Santori, E. A.;
39
40 Lewis, N. S. Solar Water Splitting Cells. *Chem. Rev.* **2010**, 110, 6446.
41
42
43
44 (9) Kay, A.; Cesar, I.; Grätzel, M. New Benchmark for Water Photooxidation by
45
46 Nanostructured Alpha-Fe₂O₃ Films. *J. Am. Chem. Soc.* **2006**, 128, 15714–15721.
47
48
49
50 (10) Choi, S. K.; Choi, W.; Park, H. Solar Water Oxidation Using Nickel-Borate Coupled
51
52 BiVO₄ Photoelectrodes. *Phys. Chem. Chem. Phys.* **2013**, 15, 6499.
53
54
55
56 (11) Yang, J.-S.; Liao, W.-P.; Wu, J.-J. Morphology and Interfacial Energetics Controls for
57
58 Hierarchical Anatase/rutile TiO₂ Nanostructured Array for Efficient Photoelectrochemical
59
60

- 1
2
3 Water Splitting. *ACS Appl. Mater. Interfaces* **2013**, *5*, 7425–7431.
4
5
6
7 (12) Mi, Q.; Ping, Y.; Li, Y.; Cao, B.; Brunshwig, B. S.; Khalifah, P. G.; Galli, G. A.; Gray,
8 H. B.; Lewis, N. S. Thermally Stable N(2)-Intercalated WO(3) Photoanodes for Water
9 Oxidation. *J. Am. Chem. Soc.* **2012**, *134*, 18318.
10
11
12
13
14 (13) Kim, J. K.; Shin, K.; Cho, S. M.; Lee, T.-W.; Park, J. H. Synthesis of Transparent
15 Mesoporous Tungsten Trioxide Films with Enhanced Photoelectrochemical Response:
16 Application to Unassisted Solar Water Splitting. *Energy Environ. Sci.* **2011**, *4*, 1465.
17
18
19
20
21
22 (14) Pesci, F. M.; Cowan, A. J.; Alexander, B. D.; Durrant, J. R.; Klug, D. R. Charge Carrier
23 Dynamics on Mesoporous WO₃ during Water Splitting. *J. Phys. Chem. Lett.* **2011**, *2*,
24 1900.
25
26
27
28
29
30 (15) Rao, P. M.; Cho, I. S.; Zheng, X. Flame Synthesis of WO₃ Nanotubes and Nanowires for
31 Efficient Photoelectrochemical Water-Splitting. *Proc. Combust. Inst.* **2013**, *34*, 2187.
32
33
34
35
36 (16) Dias, P.; Lopes, T.; Meda, L.; Andrade, L.; Mendes, A. Photoelectrochemical Water
37 Splitting Using WO₃ Photoanodes: The Substrate and Temperature Roles. *Phys. Chem.*
38 *Chem. Phys.* **2016**, *18*, 5232–5243.
39
40
41
42
43
44 (17) Liu, X.; Wang, F.; Wang, Q. Nanostructure-Based WO₃ Photoanodes for
45 Photoelectrochemical Water Splitting. *Phys. Chem. Chem. Phys.* **2012**, *14*, 7894.
46
47
48
49
50 (18) Fabrega, C.; Murcia-Lopez, S.; Monllor-Satoca, D.; Prades, J. D.; Hernandez-Alonso, M.
51 D.; Penelas, G.; Morante, J. R.; Andreu, T. Efficient WO₃ Photoanodes Fabricated by
52 Pulsed Laser Deposition for Photoelectrochemical Water Splitting with High Faradaic
53 Efficiency. *Appl. Catal. B Environ.* **2016**, *189*, 133–140.
54
55
56
57
58
59
60

- 1
2
3
4
5
6
7
8
9
10
11
12
13
14
15
16
17
18
19
20
21
22
23
24
25
26
27
28
29
30
31
32
33
34
35
36
37
38
39
40
41
42
43
44
45
46
47
48
49
50
51
52
53
54
55
56
57
58
59
60
- (19) Sarnowska, M.; Bienkowski, K.; Barczuk, P. J.; Solarska, R.; Augustynski, J. Highly Efficient and Stable Solar Water Splitting at (Na)WO₃ Photoanodes in Acidic Electrolyte Assisted by Non-Noble Metal Oxygen Evolution Catalyst. *Adv. Energy Mater.* **2016**, *6*, 1–6.
- (20) Ma, Y.; Kafizas, A.; Pendlebury, S. R.; Le Formal, F.; Durrant, J. R. Photoinduced Absorption Spectroscopy of CoPi on BiVO₄: The Function of CoPi during Water Oxidation. *Adv. Funct. Mater.* **2016**, *26*, 4951–4960.
- (21) Ma, Y.; Le Formal, F.; Kafizas, A.; Pendlebury, S. R.; Durrant, J. R. Efficient Suppression of Back Electron/hole Recombination in Cobalt Phosphate Surface-Modified Undoped Bismuth Vanadate Photoanodes. *J. Mater. Chem. A* **2015**, *3*, 20649.
- (22) Pendlebury, S. R.; Wang, X.; Le Formal, F.; Cornuz, M.; Kafizas, A.; Tilley, S. D.; Grätzel, M.; Durrant, J. R. Ultrafast Charge Carrier Recombination and Trapping in Hematite Photoanodes under Applied Bias. *J. Am. Chem. Soc.* **2014**, *136*, 9854–9857.
- (23) Zheng, J.; Sheng, W.; Zhuang, Z.; Xu, B.; Yan, Y. Universal Dependence of Hydrogen Oxidation and Evolution Reaction Activity of Platinum-Group Metals on pH and Hydrogen Binding Energy. *Sci. Adv.* **2016**, *2*, e1501602.
- (24) Brillet, J.; Yum, J.-H.; Cornuz, M.; Hisatomi, T.; Solarska, R.; Augustynski, J.; Graetzel, M.; Sivula, K. Highly Efficient Water Splitting by a Dual-Absorber Tandem Cell. *Nat. Photonics* **2012**, *6*, 824–828.
- (25) Saito, R.; Miseki, Y.; Sayama, K. Photoanode Characteristics of Multi-Layer Composite BiVO₄ Thin Film in a Concentrated Carbonate Electrolyte Solution for Water Splitting. *J.*

- 1
2
3
4
5
6
7
8
9
10
11
12
13
14
15
16
17
18
19
20
21
22
23
24
25
26
27
28
29
30
31
32
33
34
35
36
37
38
39
40
41
42
43
44
45
46
47
48
49
50
51
52
53
54
55
56
57
58
59
60
- Photochem. Photobiol. A Chem.* **2013**, *258*, 51.
- (26) Su, J.; Guo, L.; Bao, N.; Grimes, C. A. Nanostructured WO₃/BiVO₄ Heterojunction Films for Efficient Photoelectrochemical Water Splitting. *Nano Lett.* **2011**, *11*, 1928.
- (27) Rao, P. M.; Cai, L.; Liu, C.; Cho, I. S.; Lee, C. H.; Weisse, J. M.; Yang, P.; Zheng, X. Simultaneously Efficient Light Absorption and Charge Separation in WO₃/BiVO₄ Core/Shell Nanowire Photoanode for Photoelectrochemical Water Oxidation. *Nano Lett.* **2014**, *14*, 1099–1105.
- (28) Sivula, K.; Formal, F. Le; Grätzel, M. WO₃–Fe₂O₃ Photoanodes for Water Splitting: A Host Scaffold, Guest Absorber Approach. *Chem. Mater.* **2009**, *21*, 2862–2867.
- (29) Wang, W.; Dong, J.; Ye, X.; Li, Y.; Ma, Y.; Qi, L. Heterostructured TiO₂ Nanorod@Nanobowl Arrays for Efficient Photoelectrochemical Water Splitting. *Small* **2016**, *12*, 1469–1478.
- (30) Choy, K. Chemical Vapour Deposition of Coatings. *Prog. Mater. Sci.* **2003**, *48*, 57.
- (31) Chakrapani, V.; Thangala, J.; Sunkara, M. K. WO₃ and W₂N Nanowire Arrays for Photoelectrochemical Hydrogen Production. *Int. J. Hydrogen Energy* **2009**, *34*, 9050–9059.
- (32) Zhang, X.; Lu, X.; Shen, Y.; Han, J.; Yuan, L.; Gong, L.; Xu, Z.; Bai, X.; Wei, M.; Tong, Y.; et al. Three-Dimensional WO₃ Nanostructures on Carbon Paper: Photoelectrochemical Property and Visible Light Driven Photocatalysis. *Chem. Commun.* **2011**, *47*, 5804.
- (33) Ling, M.; Blackman, C. Growth Mechanism of Planar or Nanorod Structured Tungsten

- 1
2
3 Oxide Thin Films Deposited via Aerosol Assisted Chemical Vapour Deposition
4 (AACVD). *Phys. Status Solidi C* **2015**, *877*, 869–877.
5
6
7
8
9 (34) Navío, C.; Vallejos, S.; Stoycheva, T.; Llobet, E.; Correig, X.; Snyders, R.; Blackman, C.;
10 Umek, P.; Ke, X.; Van Tendeloo, G.; et al. Gold Clusters on WO₃ Nanoneedles Grown
11 via AACVD: XPS and TEM Studies. *Mater. Chem. Phys.* **2012**, *134*, 809.
12
13
14
15
16
17 (35) Toby, B. H. EXPGUI, a Graphical User Interface for GSAS. *J. Appl. Crystallogr.* **2001**,
18 *34*, 210–213.
19
20
21
22 (36) Casa Software Ltd <http://www.casaxps.com/> (accessed Nov 21, 2016).
23
24
25
26 (37) Briggs, D.; Seah, M. P. *Practical Surface Analysis by Auger and X-Ray Photoelectron*
27 *Spectroscopy*; 2nd editio.; John Wiley and Sons: Chichester, 1992.
28
29
30
31 (38) Woodward, P. M.; Sleight, A. W.; Vogt, T. Structure Refinement of Triclinic Tungsten
32 Trioxide. *J. Phys. Chem. Solids* **1995**, *56*, 1305–1315.
33
34
35
36
37 (39) Nefedov, V. I.; Firsov, M. N.; Shaplygin, I. S. Electronic Structures of MRhO₂, MRh₂O₄,
38 RhMO₄ and Rh₂MO₆ on the Basis of X-Ray Spectroscopy and ESCA Data. *J. Electron*
39 *Spectros. Relat. Phenomena* **1982**, *26*, 65–78.
40
41
42
43
44
45 (40) Tauc, J. Optical Properties and Electronic Structure of Amorphous Ge and Si. *Mater. Res.*
46 *Bull.* **1968**, *3*, 37–46.
47
48
49
50 (41) Izgorodin, A.; Izgorodina, E.; MacFarlane, D. R. Low Overpotential Water Oxidation to
51 Hydrogen Peroxide on a MnO_x Catalyst. *Energy Environ. Sci.* **2012**, *5*, 9496.
52
53
54
55
56 (42) Hong, S. J.; Jun, H.; Borse, P. H.; Lee, J. S. Size Effects of WO₃ Nanocrystals for
57
58
59
60

- 1
2
3 Photooxidation of Water in Particulate Suspension and Photoelectrochemical Film
4 Systems. *Int. J. Hydrogen Energy* **2009**, *34*, 3234–3242.
5
6
7
8
9 (43) Su, J.; Feng, X.; Sloppy, J. D.; Guo, L.; Grimes, C. A. Vertically Aligned WO₃ Nanowire
10 Arrays Grown Directly on Transparent Conducting Oxide Coated Glass: Synthesis and
11 Photoelectrochemical Properties. *Nano Lett.* **2011**, *11*, 203–208.
12
13
14
15
16 (44) Heli Wang; Torbjörn Lindgren; Jianjun He; Hagfeldt, A.; Lindquist, S.-E.
17 Photoelectrochemistry of Nanostructured WO₃ Thin Film Electrodes for Water
18 Oxidation: Mechanism of Electron Transport. *J. Phys. Chem. B* **2000**, *104*, 5686–5696.
19
20
21
22
23
24 (45) Wang, G.; Lu, X.; Li, Y. Low-Cost Nanomaterials for Photoelectrochemical Water
25 Splitting. In *Low-cost Nanomaterials - Toward Greener and More Efficient Energy*
26 *Applications*; 2014; pp. 267–295.
27
28
29
30
31
32 (46) Jin, T.; Diao, P.; Xu, D.; Wu, Q. High-Aspect-Ratio WO₃ Nanoneedles Modified with
33 Nickel-Borate for Efficient Photoelectrochemical Water Oxidation. *Electrochim. Acta*
34 **2013**, *114*, 271–277.
35
36
37
38
39
40 (47) Lhermitte, C. R.; Garret Verwer, J.; Bartlett, B. M. Improving the Stability and Selectivity
41 for the Oxygen-Evolution Reaction on Semiconducting WO₃ Photoelectrodes with a
42 Solid-State FeOOH Catalyst. *J. Mater. Chem. A* **2016**, *4*, 2960–2968.
43
44
45
46
47
48 (48) Hill, J. C.; Choi, K. Effect of Electrolytes on the Selectivity and Stability of N-Type WO₃
49 Photoelectrodes for Use in Solar Water Oxidation. *J. Phys. Chem. C* **2012**, *116*, 7612–
50 7620.
51
52
53
54
55
56 (49) Pihosh, Y.; Turkevych, I.; Mawatari, K.; Uemura, J.; Kazoe, Y.; Kosar, S.; Makita, K.;
57
58
59
60

- 1
2
3 Sugaya, T.; Matsui, T.; Fujita, D.; et al. Photocatalytic Generation of Hydrogen by Core-
4 Shell WO₃/BiVO₄ Nanorods with Ultimate Water Splitting Efficiency. *Sci. Rep.* **2015**, *5*,
5 11141.
6
7
8
9
10
11 (50) Mi, Q.; Zhanaidarova, A.; Brunschwig, B. S.; Gray, H. B.; Lewis, N. S. No Title. *Energy*
12 *Environ. Sci.* **2012**, *5*, 5694–5700.
13
14
15
16
17 (51) Seabold, J.; Choi, K.-S. No Title. *Chem. Mater.* **2011**, *23*, 1105–1112.
18
19
20 (52) Bryant, D.; Aristidou, N.; Pont, S.; Sanchez-Molina, I.; Chotchunangatchaval, T.;
21 Wheeler, S.; Durrant, J. R.; Haque, S. A. Light and Oxygen Induced Degradation Limits
22 the Operational Stability of Methylammonium Lead Triiodide Perovskite Solar Cells.
23 *Energy Environ. Sci.* **2016**, *9*, 1655–1660.
24
25
26
27
28
29
30 (53) Chen, Y.-S.; Manser, J. S.; Kamat, P. V. All Solution-Processed Lead Halide Perovskite-
31 BiVO₄ Tandem Assembly for Photolytic Solar Fuels Production. *J. Am. Chem. Soc.* **2015**,
32 *137*, 974–981.
33
34
35
36
37
38
39
40

41 SYNOPSIS: Solar water splitting is a promising solution for the renewable production of
42 hydrogen as an energy vector. Nanostructured photoelectrodes show the highest water splitting
43 efficiencies, but lack scalable routes for commercial scale-up. Here we report a direct and
44 scalable route to the single step fabrication of WO₃ nano-needle structure photoanodes. When
45 coupled with a photovoltaic device, we predict a solar-to-hydrogen efficiency of *ca* 1 %.
46
47
48
49
50
51
52
53

54 TOC graphic:
55
56
57
58
59
60

